

# All-weather Multi-Modality Image Fusion: Unified Framework and 100k Benchmark

Xilai Li, Wuyang Liu, Xiaosong Li, Fuqiang Zhou, Huafeng Li, Feiping Nie

**Abstract**—Multi-modality image fusion (MMIF) combines complementary information from different image modalities to provide a more comprehensive and objective interpretation of scenes. However, existing MMIF methods lack the ability to resist different weather interferences in real-world scenes, preventing them from being useful in practical applications such as autonomous driving. To bridge this research gap, we proposed an all-weather MMIF model. Achieving effective multi-tasking in this context is particularly challenging due to the complex and diverse nature of weather conditions. A key obstacle lies in the 'black box' nature of current deep learning architectures, which restricts their multi-tasking capabilities. To overcome this, we decompose the network into two modules: a fusion module and a restoration module. For the fusion module, we introduce a learnable low-rank representation model to decompose images into low-rank and sparse components. This interpretable feature separation allows us to better observe and understand images. For the restoration module, we propose a physically-aware clear feature prediction module based on an atmospheric scattering model that can deduce variations in light transmittance from both scene illumination and reflectance. We also construct a large-scale multi-modality dataset with 100,000 image pairs across rain, haze, and snow conditions, covering various degradation levels and diverse scenes to thoroughly evaluate image fusion methods in adverse weather. Experimental results in both real-world and synthetic scenes show that the proposed algorithm excels in detail recovery and multi-modality feature extraction. The code is available at <https://github.com/xilai/AWFusion>.

**Index Terms**—Image fusion, adverse weather, multi-modality benchmark, image restoration.

## I. INTRODUCTION

INFRARED and visible image fusion (IVIF) is performed to integrate the complementary and salient feature information from different modal images to achieve a more comprehensive interpretation of a target scene. By integrating data from different spectral ranges, IVIF contributes to advancements in

computer vision tasks [1]–[5], including semantic segmentation [6]–[8], object detection [9]–[11], and unmanned driving [12]. Recently, deep learning (DL) has exhibited remarkable progress within the realm of artificial intelligence owing to its exceptional aptitude for intricate nonlinear approximations and adeptness in extracting salient features. Consequently, several highly efficient algorithms tailored to the IVIF domain have been developed. These algorithms can be broadly categorized into three groups: generative adversarial networks (GAN)-based models [13]–[16], autoencoder (AE)-based models [2], [17], [18], and algorithmic expansion models [4], [19].

Each of these methodologies has achieved commendable outcomes in the IVIF field. However, there are three key questions that remain unresolved.

- Currently, there is a critical research gap in that IVIF cannot deliver robust scene information under adverse weather conditions. Addressing this challenge requires more than isolated algorithmic solutions for specific weather-related issues, necessitating a unified framework to comprehensively restore intricate scene details affected by adverse weather.
- The network design of most current DL-based methods, primarily developed through empirical and experiential approaches, lacks interpretability due to their black-box nature. As a result, identifying an appropriate framework often becomes a time-consuming process.
- Generally, DL-based algorithms are driven by data. Existing datasets dedicated to collecting comprehensive imaging data from multiple modalities are complete in terms of scene diversity. However, no large datasets have been developed specifically for research on applying IVIF to scenarios with adverse weather conditions. Even if certain datasets can cover scenes affected by rain and haze, their limited data make it difficult to employ them for training in joint image restoration and fusion.

To address above challenges, we propose an all-weather MMIF algorithm (AWFusion) that integrates both deweathering and fusion functions within a single framework, thereby providing an effective means to achieve robust fusion under adverse weather conditions. Compared to the traditional two-stage strategy of 'restoration+ fusion' for addressing adverse weather fusion problems, we propose that an end-to-end framework, which prioritizes modality information interaction before feature recovery, can yield more effective results. The two-stage approach has notable drawbacks: because image restoration and fusion are independent processes, errors introduced during restoration directly impact the fusion outcome.

This research was supported by the Basic and Applied Basic Research of Guangdong Province under Grant 2023A1515140077, the Natural Science Foundation of Guangdong Province under Grant 2024A1515011880, and the National Natural Science Foundation of China under Grant 62201149. The first two authors made the same contributions. (Corresponding author: Xiaosong Li.)

Xilai Li, Wuyang Liu and Xiaosong Li are with the School of Physics and Optoelectronic Engineering, Foshan University, Foshan 528225, China. (emails: 20210300236@stu.fosu.edu.cn; lixiaosong@buaa.edu.cn).

Fuqiang Zhou is with the School of Instrumentation and Optoelectronic Engineering, Beihang University, Beijing 100083, China (e-mail: zfq@buaa.edu.cn).

Huafeng Li is with the School of Information Engineering and Automation, Kunming University of Science and Technology, China. (e-mail: hfchina99@163.com).

Feiping Nie is with the School of Artificial Intelligence, Optics and Electronics (iOPEN), School of Computer Science, Northwestern Polytechnical University, China. (email: feipingnie@gmail.com).

Additionally, the lack of correlation between these tasks means that while efficient restoration may enhance fusion performance, the reverse is not true.

In complex natural scenes, images often contain substantial redundant information, allowing for the inference of the original scene even when the image quality is degraded due to adverse weather conditions. From a network learning perspective, deep neural networks extract features at different levels through layer-by-layer feature extraction operations. Early layers capture low-level features such as edges, textures, and color gradients, while deeper layers learn more complex semantic information and scene structures. However, the loss of low-level features does not entirely compromise high-level scene information. The network can reconstruct the overall scene from remaining valid pixels or local features. Therefore, we argue that it is not necessary to perform image restoration first when handling complex scenes. Second, the task of multi-modality image fusion inherently involves discarding redundant information and retaining complementary data. Unlike image restoration, which aims to recover as much detail as possible without accounting for redundancy, fusion emphasizes retaining only the most significant information. By leveraging complementary multi-modality features, the network can concentrate on these useful details during reconstruction, rather than processing unnecessary pixel data. This not only reduces computational complexity but also enhances the ability of the network to recover the aspects of the scene that best represent its true characteristics. Thus, our objective is to shift the focus of the network from perfect pixel-level recovery to maximizing the representation of key scene information.

The fusion module was constructed to equip the network with the ability to extract multi-modality information, isolate the shared and unique features of each modality, and fuse them based on a unique prior for each feature type. Firstly, we introduce a learned low-rank representation (LLRR) block [4] to decompose the source images into sparse and low-rank components. This feature decoupling approach allows for a more comprehensive consideration of the feature information of the image. Additionally, the low-rank and sparse decompositions reduce the computational complexity of the fusion module. The low-rank component, with its fewer degrees of freedom, represents the global structure with fewer parameters, while the sparse component focuses on a limited number of salient pixels, minimizing unnecessary computational overhead. By leveraging this decomposition, more efficient algorithms can be applied to process large-scale images. For the features integration, a sparse feature prediction module based on an optimization model was proposed to reconstruct the sparse components, and a sparse transformer [20] was introduced to capture the long-range contextual information of an image.

In the restoration module, the clear feature prediction block was developed, guided by the atmospheric scattering model [21], [22]. This module derives illumination and reflectance features from images to predict the distribution of light transmission, utilizing learned convolutional sparse coding (LCSC) [23]. Thus, propelled by both mathematical optimization algorithms and physical models, our proposed model has interpretable and physically-aware properties. It obviates the

necessity for model customization to cater to specific weather-related issues, and it enables the simultaneous training of multiple teacher networks under a unified framework for a singular weather restoration task. Subsequently, distillation learning was incorporated into the model to transfer knowledge from these diverse teacher networks to a singular student network, enabling the model to resolve degradation issues stemming from various severe weather phenomena.

Furthermore, we introduce a large-scale benchmark, AWMM-100k, specifically designed for multi-modality image fusion in adverse weather conditions, aiming to advance research in this challenging field. Our dataset consists of 100,000 multi-modality image pairs, comprehensively covering both synthetic and real-world scenes affected by three major weather degradations: rain, haze, and snow. To ensure robust evaluation, the data spans multiple degradation levels for each weather type, capturing the diversity and complexity of natural environments. This benchmark addresses a critical gap in the field by providing a reliable, diverse, and extensive resource for developing and evaluating fusion methods under real-world adverse weather conditions.

The contributions of this study are summarized as follows.

- We propose an end-to-end all-weather MMIF framework, effectively fusing and recovering the perturbed multi-modality information. Unlike existing MMIF works, to the best of our knowledge, this is the first work to address MMIF and adverse weather removal simultaneously, defining a new challenging task.
- We propose a feature separation-based fusion module that considers the reconstruction of local and global features from sparse and low-rank components.
- We propose a physically-aware clear feature prediction block (PFB) that comprehensively accounts for the restoration of clear features, thereby avoiding a time-consuming empirical network design.
- Leveraging both existing MMIF datasets and our collected data, we built a dataset (AWMM-100k) dedicated to MMIF research under adverse weather. It containing 100,000 aligned infrared and visible image pairs with labels for object detection, establishing it as a versatile benchmark for a broad spectrum of vision tasks.

## II. RELATED WORK

### A. DL-based MMIF Methods

DL-based IVIF algorithms [24]–[31] demonstrate robust fusion performance in conventional scenes, employing methodologies such as GAN or AE to effectively integrate salient feature information from each modality. With the widespread utilization of IVIF technology, researchers increasingly integrate this technology into downstream vision tasks [3], [32]–[35]. Their aim is to enhance the extraction of multi-modality features, augmenting semantic information and leveraging fused images to optimize the performance of tasks such as object detection, semantic segmentation, and salient object detection. Furthermore, there are many joint multi-tasking algorithms designed to cope with real-world applications [36]–[38]. In practical applications, images captured by cameras

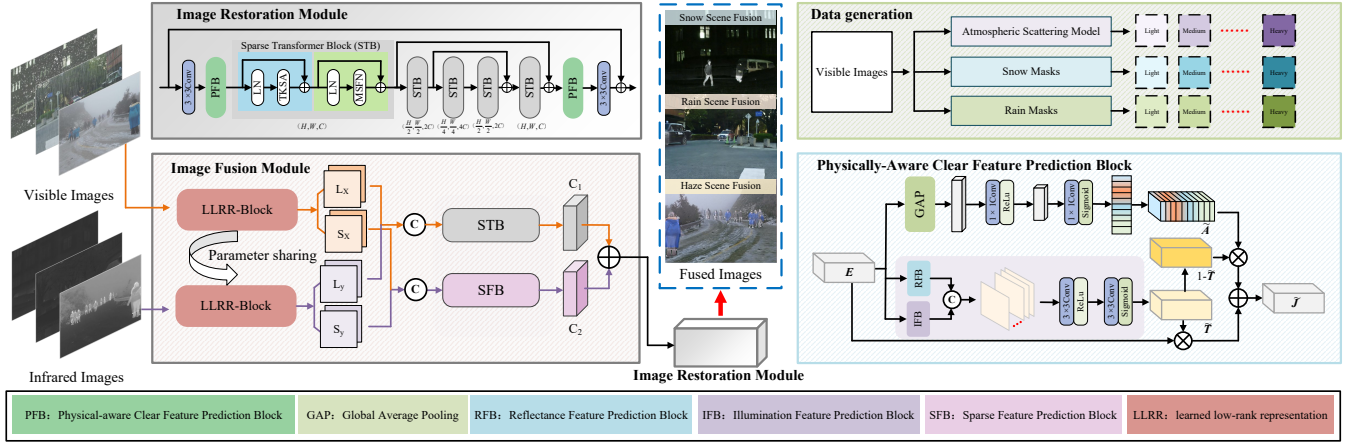


Fig. 1. The architecture of the proposed all-weather MMIF framework.

may be slightly misaligned and distorted; some researchers have designed correction networks for fusion specifically for such situations [37]. Xu et al. [38] designed an IVIF model that could fuse unaligned image pairs, effectively reducing the cost of adopting IVIF technology. In some cases, the fixed input and output resolutions of images can limit the development of IVIF-based methods; Li et al. [39] designed an IVIF framework specifically for this problem. In addition, some algorithms apply the IVIF task to degraded environments, such as noise [40], low light [41], and low contrast scenes [42]. However, current research does not effectively address the generalization of IVIF algorithms, whether they are single-task or multi-task, to adverse weather conditions.

### III. PROPOSED METHOD

#### A. Overview

As shown in the Fig. 1, AWFusion comprises two main parts: image fusion and image restoration. It is important to emphasize that the proposed algorithm is trained in an end-to-end manner. First, the multi-modality data affected by adverse weather is sent to the image fusion module for feature encoding. To effectively distinguish private and shared features from different modalities and thereby allow the fusion network to overcome the limitations in using a single encoder, a LLRR block is introduced. This block decomposes the source image into a low-rank component, which captures global structural information with high pixel correlation, and a sparse component, which represents high-frequency information with faster pixel variations. This approach enables the targeted handling of specific modal features and enhances fusion outcomes.

In the second part, the multi-modality interaction features obtained from the fusion module are fed into the restoration module to infer the original clear scene. As shown in Fig. 1, the restoration module in the model uses a U-Net backbone. In the backbone network, we stack five sparse transformer blocks (STB) to extract useful features distributed in adverse weather. STB mainly consist of top-k sparse attention (TKSA) and mixed-scale feed-forward network (MSFN). Regarding TKSA, it performs feature aggregation to keep the features in an

image sparse, and MSFN extracts multiscale local information from the image [20]. The proposed PFB focuses on refining the spatial information, which is embedded into both sides of the backbone network and enforced before being inputted into subsequent modules, which helps recover the detailed information. Finally, the reconstructed fusion results are output through the restoration module.

Finally, drawing inspiration from Che et al. [43], we introduced a distillation learning approach in which distinct teacher models are initially trained for individual weather-related issues. Subsequently, knowledge is collaboratively transferred from these multiple teacher models to student models to comprehensively address weather-related challenges.

#### B. Image Fusion Module

Through the decomposition provided by the LLRR block, our network focuses solely on the fusion of low-rank and sparse features. Low-rank components reflect the global information and main structure of the image, constrained by certain rank features. Given the strong ability of Transformer to capture global context, we employ the STB to fuse low-rank features from different modalities. In contrast, sparse components represent local details such as edges, textures, and high-frequency information. To effectively manage these local fusions, we design the Sparse Feature Block (SFB).

1) *SFB*: Sparse feature fusion is performed to effectively extract and integrate local features specific to an infrared image ( $IR$ ) and a visible image ( $Vis$ ). The fused feature map  $\tilde{Z}$  consists of two parts: the sparse feature  $s_{I,k} \in \mathbb{R}^{H \times W \times K}$  for  $IR$  and the sparse feature  $s_{V,k} \in \mathbb{R}^{H \times W \times K}$  for  $Vis$ .  $\tilde{Z}$  is modeled as follows:

$$\tilde{Z} = \sum_k g_k^{S_I} * s_{I,k} + \sum_k g_k^{S_V} * s_{V,k} \quad (1)$$

where  $\{g_k^{S_I}\}_{k=1}^K \in \mathbb{R}^{s \times s \times K}$  and  $\{g_k^{S_V}\}_{k=1}^K \in \mathbb{R}^{s \times s \times K}$  are the sparse filters of  $\tilde{Z}$  related to  $IR$  and  $Vis$ , respectively, and

$K$  denotes the number of filters. Subsequently, Eq. (1) can be transformed into the following optimization problem:

$$\begin{aligned} & \text{Argmin}_{S_I^I, S_V^V} \frac{1}{2} \left\| IR - \sum_k (g_k^{S_I} * s_{I,k}) \right\|_2^2 \\ & + \frac{1}{2} \left\| Vis - \sum_k (g_k^{S_V} * s_{V,k}) \right\|_2^2 + \lambda \sum_k (\|s_{I,k}\|_1 + \|s_{V,k}\|_1) \end{aligned} \quad (2)$$

Similar to [19],  $s_{I,k}$  and  $s_{V,k}$  are solved as follows:

$$S_{j+1}^I = S_\lambda(S_j^I - L_{S_I} * C_{S_I} * S_j^I + L_{S_I} * IR) \quad (3)$$

$$S_{j+1}^V = S_\lambda(S_j^V - L_{S_V} * C_{S_V} * S_j^V + L_{S_V} * Vis) \quad (4)$$

where  $S_I \in \mathbb{R}^{H \times W \times K}$  and  $S_V \in \mathbb{R}^{H \times W \times K}$  are the stack of feature responses  $\{s_{I,k}\}_{k=1}^K$  and  $\{s_{V,k}\}_{k=1}^K$  respectively;  $S_j^I$  and  $S_j^V$  are the updates of  $S_I$  and  $S_V$  at the  $j$ -th iteration, respectively; and  $C_{S_I} \in \mathbb{R}^{s \times s \times K}$ ,  $C_{S_V} \in \mathbb{R}^{s \times s \times K}$ ,  $L_{S_I} \in \mathbb{R}^{s \times s \times K}$  and  $L_{S_V} \in \mathbb{R}^{s \times s \times K}$  are the learnable convolutional layers. According to LCSC, we can expand the iterations in Eq. (3) and Eq. (4) into a network as shown in the framework in Fig. 2.

### C. Image Restoration Module

The second phase aims to achieve image restoration in the presence of three types of adverse weather conditions (rain, snow, and haze). Based on the atmospheric scattering model, adverse weather conditions such as rain, haze, and snow induce scattering and absorption of light by particles in the atmosphere. Consequently, these atmospheric phenomena lead to comparable image degradation across a spectrum of unfavorable conditions [44]. For instance, during heavy rainfall, the accumulation of distant rain lines and atmospheric water particles creates a "rain curtain" effect. This visual effect of rainwater accumulation produces a haze like phenomenon in the image background [45]. The above conclusion provide a research basis to realize deweathering in the same framework. Therefore, for the restoration module, an atmospheric scattering model is combined to simulate the process of image degradation, and a PFB is proposed.

1) *PFB*: The construction of the PFB was guided by the physical mechanism of image degradation and transformation of the atmospheric scattering model. First, utilizing kernel  $k$  for feature extraction results in the following revised expression of atmospheric scattering model:

$$k * J = k * (I \odot \frac{1}{T}) + k * A - k * (A \odot \frac{1}{T}) \quad (5)$$

where  $*$  denotes the convolution operator, and  $\odot$  represents the Hadamard product. Subsequently, by introducing the matrix-vector forms of  $k$ ,  $J$ ,  $I$ ,  $A$ , and  $1/T$ , which are denoted as  $\mathbf{K}$ ,  $\mathbf{J}$ ,  $\mathbf{I}$ ,  $\mathbf{A}$ , and  $\mathbf{D}$ , respectively, Eq. (5) can be redefined as follows:

$$\mathbf{KJ} = \mathbf{KDI} + \mathbf{KA} - \mathbf{KDA} \quad (6)$$

According to [21], given the input adverse weather image feature  $\mathbf{E} \in \mathbb{R}^{H \times W \times K}$ , the clear feature  $\tilde{\mathbf{J}} \in \mathbb{R}^{H \times W \times K}$  can be computed as follows:

$$\tilde{\mathbf{J}} = \mathbf{E} \odot \tilde{\mathbf{T}} + \tilde{\mathbf{A}}(1 - \tilde{\mathbf{T}}) \quad (7)$$

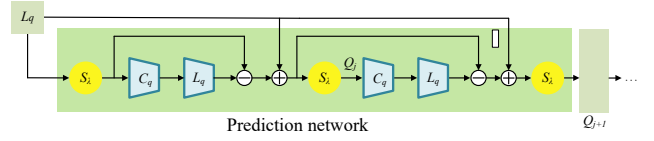


Fig. 2. Network structure of RFB, IFB, and SFB.  $q_k \in \{d_k, m_k, s_{I,k}, s_{V,k}\}$  and  $Q_j \in \{D_j, M_j, S_j^I, S_j^V\}$ .

where  $\tilde{\mathbf{A}} \in \mathbb{R}^{H \times W \times K}$  represents an approximation of the characteristic  $\mathbf{KA}$  of the atmospheric light  $A$ , and  $\tilde{\mathbf{T}} \in \mathbb{R}^{H \times W \times K}$  is a characteristic associated with the transmission map. 1 represents a matrix composed entirely of ones. Since atmospheric light is usually assumed to be homogeneous, as shown in Fig. 1, we use global average pooling to eliminate redundant information within the feature space to predict the atmospheric light feature  $\tilde{\mathbf{A}}$ .

In adverse weather conditions like dense haze, rain, or snow, light undergoes scattering and absorption, causing alterations in both image reflectance and illumination. For example, haze reduces the intensity of light reflected from objects to the camera by scattering it, with this effect being more pronounced at greater distances. Rain and snow also alter the surface reflectivity of objects when they adhere to them, affecting how light is reflected. Additionally, atmospheric particles can cause light to be reflected, refracted, and absorbed, impacting the overall illumination of the scene. Consequently, for the prediction of the feature  $\tilde{\mathbf{T}}$ , by analyzing changes in reflectance and illumination of objects in an image, we can infer changes in light transmission, thus realizing estimation of the image transmission information.

We disassemble  $\tilde{\mathbf{T}}$  into a combination of reflectance  $d_k \in \mathbb{R}^{H \times W \times K}$  and illumination  $m_k \in \mathbb{R}^{H \times W \times K}$  features, which is modeled as follows:

$$\tilde{\mathbf{T}} = \sum_k g_k^d * d_k + \sum_k g_k^m * m_k \quad (8)$$

where  $\{g_k^d\}_{k=1}^K \in \mathbb{R}^{s \times s \times K}$  and  $\{g_k^m\}_{k=1}^K \in \mathbb{R}^{s \times s \times K}$  are the reflectance and illumination filters of  $\tilde{\mathbf{T}}$ , respectively. Subsequently, we compute the reflectance and illumination feature responses  $\{d_k, m_k\}_{k=1}^K$  by solving the following optimization problem:

$$\begin{aligned} & \text{Argmin}_{d_k, m_k} \frac{1}{2} \left\| I - \sum_k (g_k^d * d_k) \right\|_2^2 \\ & + \frac{1}{2} \left\| I - \sum_k (g_k^m * m_k) \right\|_2^2 + \lambda \sum_k (\|d_k\|_1 + \|m_k\|_1) \end{aligned} \quad (9)$$

a) *Reflectance Feature Prediction Block (RFB)*: The goal of RFB is used to compute the reflectance feature. According to [19], we fix  $m_k$  to update  $d_k$  by rewriting Eq. (9) as:

$$\text{Argmin}_{d_k} \frac{1}{2} \left\| I - \sum_k (g_k^d * d_k) \right\|_2^2 + \lambda \sum_k \|d_k\|_1 \quad (10)$$

Eq. (10) is a standard convolutional sparse coding problem that can be solved using LCSC [23] by rewriting Eq. (10) as:

$$D_{j+1} = S_\lambda (D_j - L_d * C_d * D_j + L_d * I) \quad (11)$$

where  $D \in \mathbb{R}^{H \times W \times K}$  is the stack of feature responses  $\{d^k\}_{k=1}^K$ ,  $D_j$  is the update of  $D$  at the  $j$ -th iteration,  $C_d \in \mathbb{R}^{s \times s \times K}$  and  $L_d \in \mathbb{R}^{s \times s \times K}$  are the learnable convolutional layers related to the filters  $\{g_k^d\}_{k=1}^K$ , and  $S_\lambda$  represents the soft thresholding operator. Similar to SFB, we expand the iterations in Eq. (11) into a network as shown in Fig. 2.

b) *Illumination Feature Prediction Block (IFB)*: The goal of IFB is to compute the illuminance feature in a hazy image, the structure of this network is similar to that of DFB. By fixing  $d_k$  to update  $m_k$ , Eq. (9) can be rewritten as:

$$\text{Argmin}_{m_k} \frac{1}{2} \|I - \sum_k g_k^d * m_k\|_2^2 + \lambda \sum_k \|m_k\|_1 \quad (12)$$

By using LCSC to solve the above problem, Eq. (12) can be rewritten as follows:

$$M_{j+1} = S_\lambda (M_j - L_m * C_m * M_j + L_m * I) \quad (13)$$

where  $M \in \mathbb{R}^{H \times W \times K}$  is the stack of feature responses  $\{m^k\}_{k=1}^K$ ,  $M_j$  is the update of  $M$  at the  $j$ -th iteration, and  $C_m \in \mathbb{R}^{s \times s \times K}$  and  $L_m \in \mathbb{R}^{s \times s \times K}$  are the learnable convolutional layers related to the filters  $\{g_k^m\}_{k=1}^K$ . The network structure of the IFB is shown in Fig. 2.

#### D. Loss Function

The loss function integrates two components. The first part focuses on the loss function used to ensure the quality of the fusion results, while the second part addresses the loss function constraining the generation of reflectance and illumination features. The fusion loss includes structural similarity index (SSIM), mean square error (MSE) and color consistency loss. The calculation for SSIM can be expressed as follows:

$$SSIM(X, Y) = \frac{(2\mu_X \mu_Y + C_1)(2\sigma_{XY} + C_2)}{(\mu_X^2 + \mu_Y^2 + C_1)(\sigma_X^2 + \sigma_Y^2 + C_2)} \quad (14)$$

where  $X$  and  $Y$  represents two different images. The  $\mu_Z$ , where  $Z \in X, Y$ , denotes the mean of image  $Z$ ,  $\sigma_Z$  represents the standard deviation of image  $Z$ ,  $\sigma_{XY}$  denotes the covariance between images  $X$  and  $Y$ . The constants  $C_1$  and  $C_2$  are introduced to prevent the denominator from approaching zero. Thus, the formula for the SSIM loss ( $\mathcal{L}_{SSIM}$ ) is as follow:

$$\mathcal{L}_{SSIM}(F, GT_{IR}, GT_{Vis}) = SSIM(GT_{IR}, F) + SSIM(GT_{Vis}, F) \quad (15)$$

where  $GT_{IR}$  and  $GT_{Vis}$  represent the ground truth of infrared and visible images under adverse weather, respectively. In addition, MSE can be calculated as follows:

$$MSE(X, Y) = \frac{1}{HW} \sum_{i=1}^H \sum_{j=1}^W [X(i, j) - Y(i, j)]^2 \quad (16)$$

where  $H$  and  $W$  represent the height and width of the image, respectively. The MSE loss ( $\mathcal{L}_{MSE}$ ) is as follow:

$$\mathcal{L}_{MSE}(F, GT_{IR}, GT_{Vis}) = MSE(GT_{IR}, F) + MSE(GT_{Vis}, F) \quad (17)$$

Colour consistency loss is used to ensure that the fused image maintains consistent colours with the  $Vis$ . We transform the image into the YCbCr color space and apply a constraint using the Euclidean distance between the Cb and Cr channels. This can be expressed as:

$$\mathcal{L}_{color}(F, GT_{Vis}) = \frac{1}{HW} \|\mathcal{F}_{CbCr}(F) - \mathcal{F}_{CbCr}(GT_{Vis})\|_1 \quad (18)$$

where  $\mathcal{F}_{CbCr}$  represents the transfer function from RGB to the CbCr color space.

To effectively constrain the generation of the reflectance feature  $d_k$  and the illuminance feature  $m_k$  in Eq. (8), we propose a reconstruction loss inspired by retina theory. According to this theory, a natural image can be viewed as the product of its reflectance and luminance components. Based on this principle, we reconstruct the natural image by multiplying the extracted reflectance and illuminance features, and impose the reconstruction loss using the  $GT_{Vis}$  as the reference. The reconstruction loss can be expressed as follows:

$$\mathcal{L}_{recon}(d_k, m_k, GT_{Vis}) = \|GT_{Vis} - (d_k * m_k)\|_1 \quad (19)$$

The total loss of AWFusion is denoted as:

$$\mathcal{L}_{total} = \mathcal{L}_{SSIM}(F, GT_{IR}, GT_{Vis}) + \mathcal{L}_{MSE}(F, GT_{IR}, GT_{Vis}) + \mathcal{L}_{color}(F, GT_{Vis}) + \mathcal{L}_{recon}(d_k, m_k, GT_{Vis}) \quad (20)$$

TABLE I  
OVERVIEW OF THE AWMM-100K DATASET: A LARGE-SCALE MULTI-MODALITY BENCHMARK FOR ADVERSE WEATHER CONDITIONS.

Aspect	Description
Total Image Pairs	100,000 pairs
Modalities	Visible (RGB), Infrared (IR)
Weather Conditions	Rain, Haze, Snow
Degradation Levels	Heavy, Medium, and Light
Data Types	Synthetic and Real-world Scenes
Scenes	Urban, Suburban, Rural, Natural, etc.
Task Labels	Object Detection

#### E. MMIF Benchmark for Adverse Weather

Current MMIF datasets lack comprehensive scene coverage under adverse weather. Combining existing datasets (Road-Scene [28], MSRS [46], M3FD [3], and LLVIP [47]) and our newly collected data in real-world scenes, we have established a benchmark AWMM-100k, which encompasses a diverse range of weather conditions. Each type of weather (rain, haze, and snow) is categorized into heavy, medium, and light levels. Specific descriptions are shown in Table I. The AWMM-100k dataset was collected using a DJI M30T drone, equipped with high-resolution visible and thermal imaging cameras to capture data in complex scenes.

Collecting a large amount of aligned paired multi-modality data and corresponding ground truth in real adverse weather is challenging, leading most current research to rely on synthetic data for training. Effectively degrading clean data and imbuing the model with adaptability to real scenes are pivotal for constructing benchmark. However, the degradation of infrared images in severe weather remains a current research gap. To

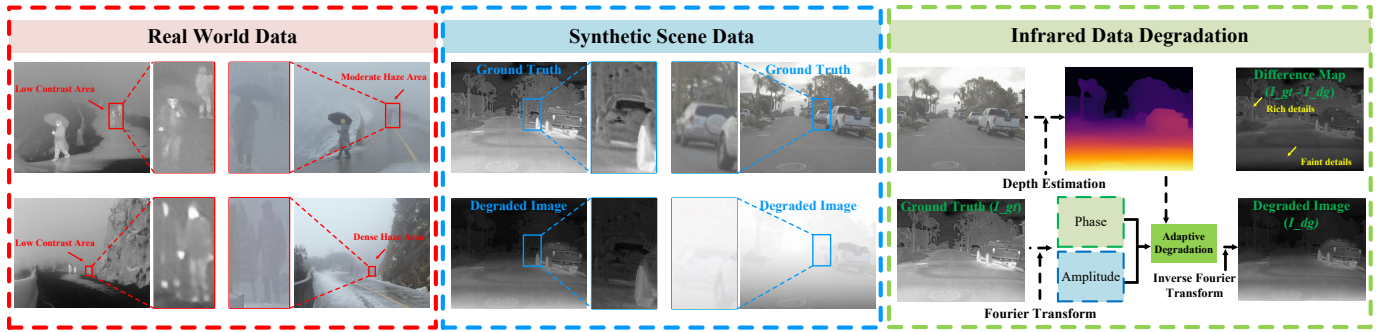


Fig. 3. Schematic representation of real-world and synthetic scene data. In this case, the data for the real scene is from AWMM-100k and the data for the synthesized scene is from the RoadScene dataset.

address this, we analyze data collected during real severe weather to determine the most effective methods for degrading infrared images. Observations of the data in Fig. 3 allow us to draw the following conclusions: 1) While the visible image exhibits degradation due to adverse weather conditions, the corresponding infrared image lacks explicit weather features, showcasing only varying degrees of degradation commensurate with the extent of image disturbance, such as diminished contrast and detail. 2) The depth of the scene affects the extent of light refraction and scattering, resulting in greater blurring in distant scenes compared to closer ones. Based on the above conclusions, we propose an adaptive degradation strategy for infrared images based on scene depth. First, we transpose the image into the Fourier domain and use the depth map as the weights for degradation. Subsequently, the weight map is normalised and multiplied with the amplitude and phase of the image respectively and then inverted to obtain the degraded image. However, distant pixels in the depth map are always represented in black, i.e., the pixel value is 0. In order to suppress too small weights, we add 0.3, 0.2 and 0.1 to points with pixel values less than 0.2 according to the three degrees of light, medium and heavy, respectively.

Degraded visible images generation process is illustrated in Fig. 1. We employ a phenomenological pipeline [48] to introduce haze into source images, while rain and snow images are generated using Photoshop software utilizing masks based approach [49]. In addition, Fig. 4 presents examples of multi-modality data captured in real-world scenarios under adverse weather. Moreover, this benchmark provides labels for object detection task. These attributes render it a versatile resource for investigating a broad spectrum of visual tasks.

## IV. EXPERIMENT

### A. Experimental Configurations

We performed fusion experiments on the AWMM-100k dataset under adverse weather (rain, haze, and snow). The experiment included ten state-of-the-art (SOTA) IVIF algorithms (U2Fusion [2], LRRNet [4], MURF [38], TIM [35], CoCoNet [50], TarDal [3], IGNet [32], DRMF [51], MUFusion [52], CrossFuse [53]). We chose nine metrics to quantitatively evaluate different fusion results: Gradient-Based Fusion Performance ( $Q_G$ ), Image Fusion Metric-Based on a Multi-scale Scheme ( $Q_M$ ), Piella's Metric ( $Q_S$ ), Chen-Blum Metric



Fig. 4. Partial real multi-modality data from AWMM-100k.

( $Q_{CB}$ ), Chen-Varshney Metric ( $Q_{CV}$ ) [1], [54],  $Q^{AB/F}$  [55], Structural Similarity Measurement ( $SSIM$ ), the Sum of the Correlations of Differences ( $SCD$ ) [56] and Entropy ( $EN$ ). For the synthesized data, the comparison method uses clean source images, while the proposed algorithm performs fusion using images affected by three different adverse weather conditions. For real scene data, both the proposed algorithm and the comparison method use the same source images. This comparison setup allows for a more effective demonstration of the performance of the proposed algorithm.

### B. Training Details

For the training process, three specialized teacher networks and one student network were trained under different weather conditions. For different adverse weather conditions, we selected 1,000 pairs of multi-modality images from the AWMM-100k dataset as the training set for the teacher network. Each image was randomly cropped to a size of  $160 \times 160$  pixels to form a batch. The initial learning rate for the Adam optimizer was set to  $1 \times 10^{-3}$ , and the model training was conducted over 300 iterations. During the knowledge transfer phase, the teacher network remained fixed while the student network was trained for 200 epochs on a mixed training set comprising three weather types. Furthermore, we employed two LLRR

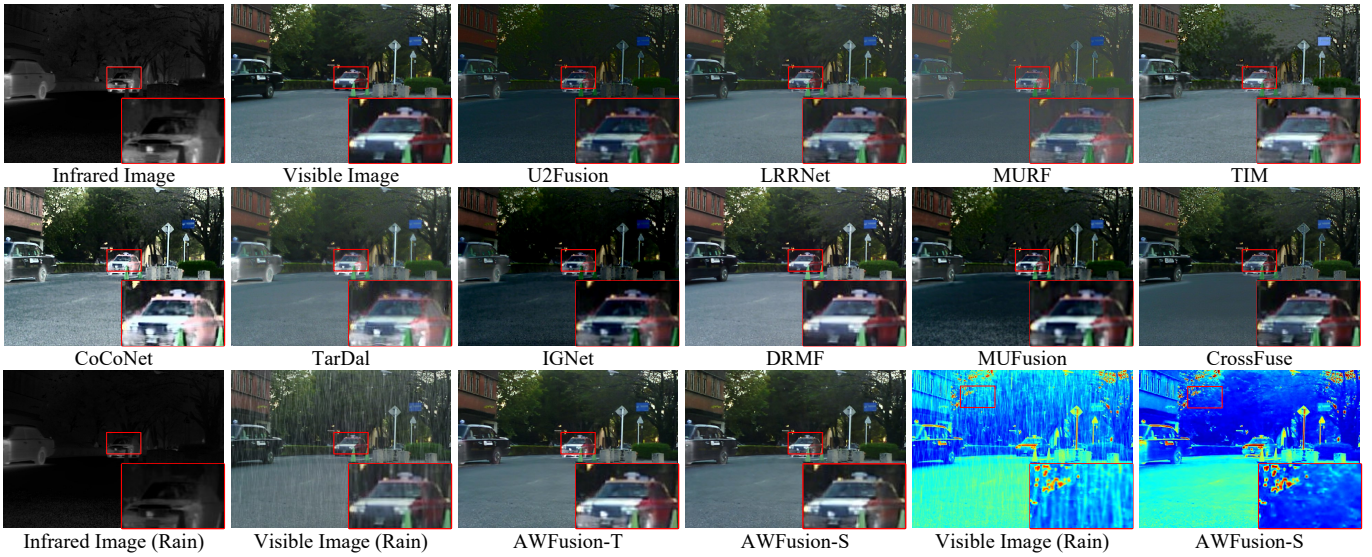


Fig. 5. Comparison of fusion results obtained by the proposed algorithm under rain weather, and the results of the comparison methods under ideal condition.

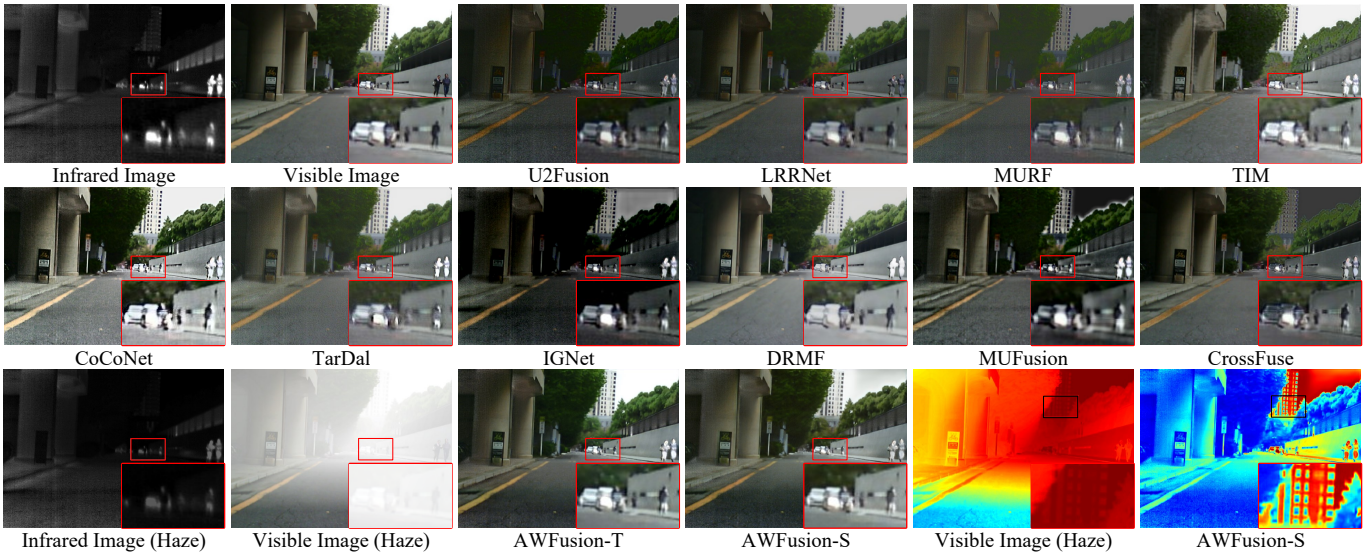


Fig. 6. Comparison of fusion results obtained by the proposed algorithm under haze weather and the results of the comparison methods under ideal condition.

blocks, while the remaining parameters were set according to the original paper. The number of LCSC blocks iterated in the RFB, IFB, and SFB models is four, with 24 filters per block. The size of the convolutional kernel used in each convolutional layer is nine. All experiments were carried out using the PyTorch framework on a system equipped with two NVIDIA 4090 GPUs.

### C. Qualitative Comparison

1) *Comparison on synthetic data:* Figs. 5 to 7 present the fusion results of different algorithms on the synthetic dataset. Notably, only the proposed algorithm performs fusion under adverse weather conditions, while the comparison methods are fused in ideal scenes. Additionally, we include pseudo-color images of the disturbed visible images and the fusion results from the student model to further demonstrate the effectiveness

of the proposed algorithm in mitigating severe weather interference. AWFusion-T and AWFusion-S represent the teacher and student models of the proposed algorithm, respectively. As shown in Figs. 5 to 7, all comparison methods achieve good fusion results in ideal scenes. Four methods—U2Fusion, LRRNet, MURF, and IGINet—produce fusion results with low contrast. In contrast, CoCoNet and MUFusion enhance the source image features, leading to some redundancy and loss of detail in the thermal radiation information in the fusion results. In daytime scenes, the TIM, TarDal, and DRMF methods effectively retain the texture information from the visible images. However, in nighttime scenes, the TarDal method exhibits a loss of detail. Additionally, both MUFusion and CrossFuse show poor color retention of the sky, introducing excessive infrared information into the region, which is not compatible with the human visual system.

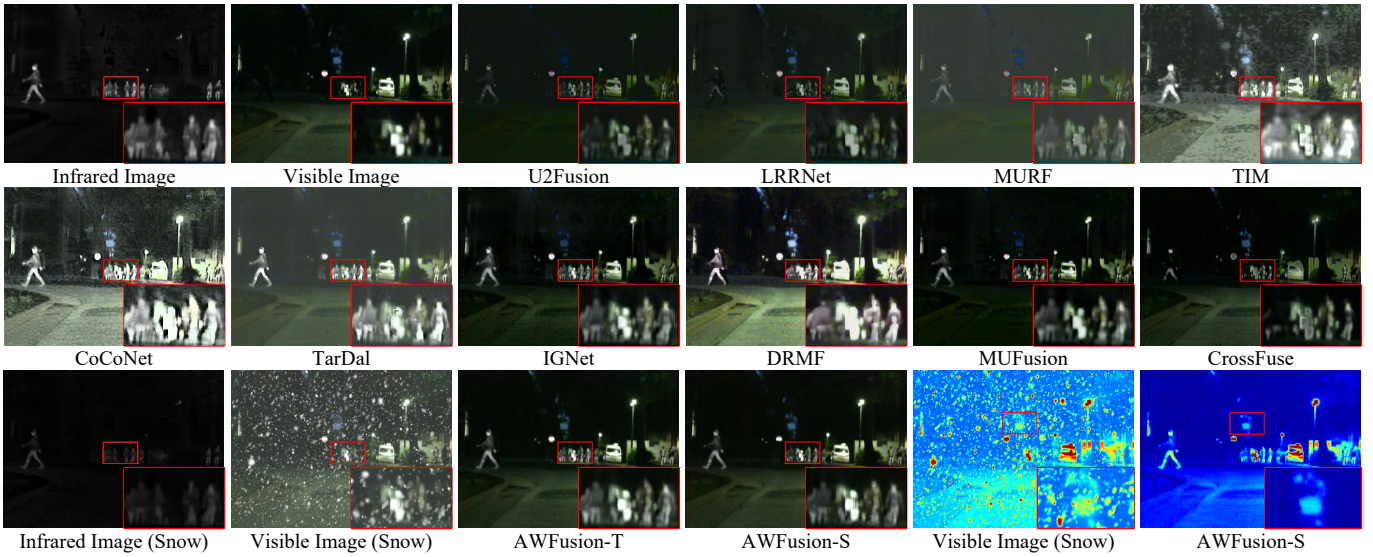


Fig. 7. Comparison of fusion results obtained by the proposed algorithm under snow weather and the results of the comparison methods under ideal condition.



Fig. 8. Results of different dehazing algorithms on real-world haze images.

Under severe weather interference, the challenge not only arises from weather-related artifacts on the visible images but also from the low contrast of infrared images and the loss of thermal radiation information. By examining the fusion results of the proposed algorithm in adverse weather conditions, we observe that it performs effective, high-quality fusion by removing interfering information from the visible image and enhancing weak targets in the scene. Additionally, in the red zoomed-in areas, the algorithm not only recovers a clean scene but also facilitates multi-modality information interactions, integrating salient details from different modalities. This results in superior performance compared to most of the comparison methods, particularly in terms of overall contrast and detail preservation. Furthermore, the pseudo-colored images show that the proposed algorithm effectively removes interference without smoothing local texture information, which is crucial for demonstrating the restoration performance of algorithm. Since the student model exhibits stronger generalization ability compared to the teacher model, some performance is sacrificed. From the experiments, we observe that the first notice-

able effect is the weakening of color information, followed by the retention of infrared information in the sky region. However, this does not affect the semantic content of the overall image, and the student model remains close to the teacher model in terms of overall contrast.

2) *Comparison on real-world data:* Fig. 9, we present the fusion results of all methods in a real haze scene. Additionally, we evaluate the fusion performance of different methods using two downstream tasks: object detection and depth estimation. We used YOLOv7 [10] as a detector and MiDas [57] as a depth estimator. Unlike synthetic data, the input images used to comparison methods and the proposed algorithm are the same, as there is no corresponding ground truth for real scene data. Furthermore, we retrained three high-performing dehaze algorithms (Dehazer [58], DehazeFormer [59], UCL-Dehaze [60]) using images from the AWMM-100K to optimize the visible images for input into the fusion comparison methods. However, as seen in Fig. 8, all dehaze methods resulted in varying degrees of color distortion, suggesting that feeding such distorted inputs into the different fusion methods could lead to unfair comparisons. Therefore, we provided all fusion methods with uniform input images.

As shown in Fig. 9, in the first set of fusion comparison tests, CoCoNet, TarDal, and MUFusion effectively retain the significant thermal radiation information from the infrared map. These three methods, which tend to enhance infrared data to achieve higher contrast, can address some challenges in real haze scenes. However, this approach excessively masks details from the visible image, preventing the recovery of clear scene details. Additionally, for pedestrians submerged in haze, DRMF and CrossFuse lose target information from the infrared image, incorrectly prioritizing the blurred pedestrian details from the visible image. In contrast, the proposed algorithm strikes an effective balance between the complementary information from different modalities, maintaining good overall scene contrast while also recovering some detail in

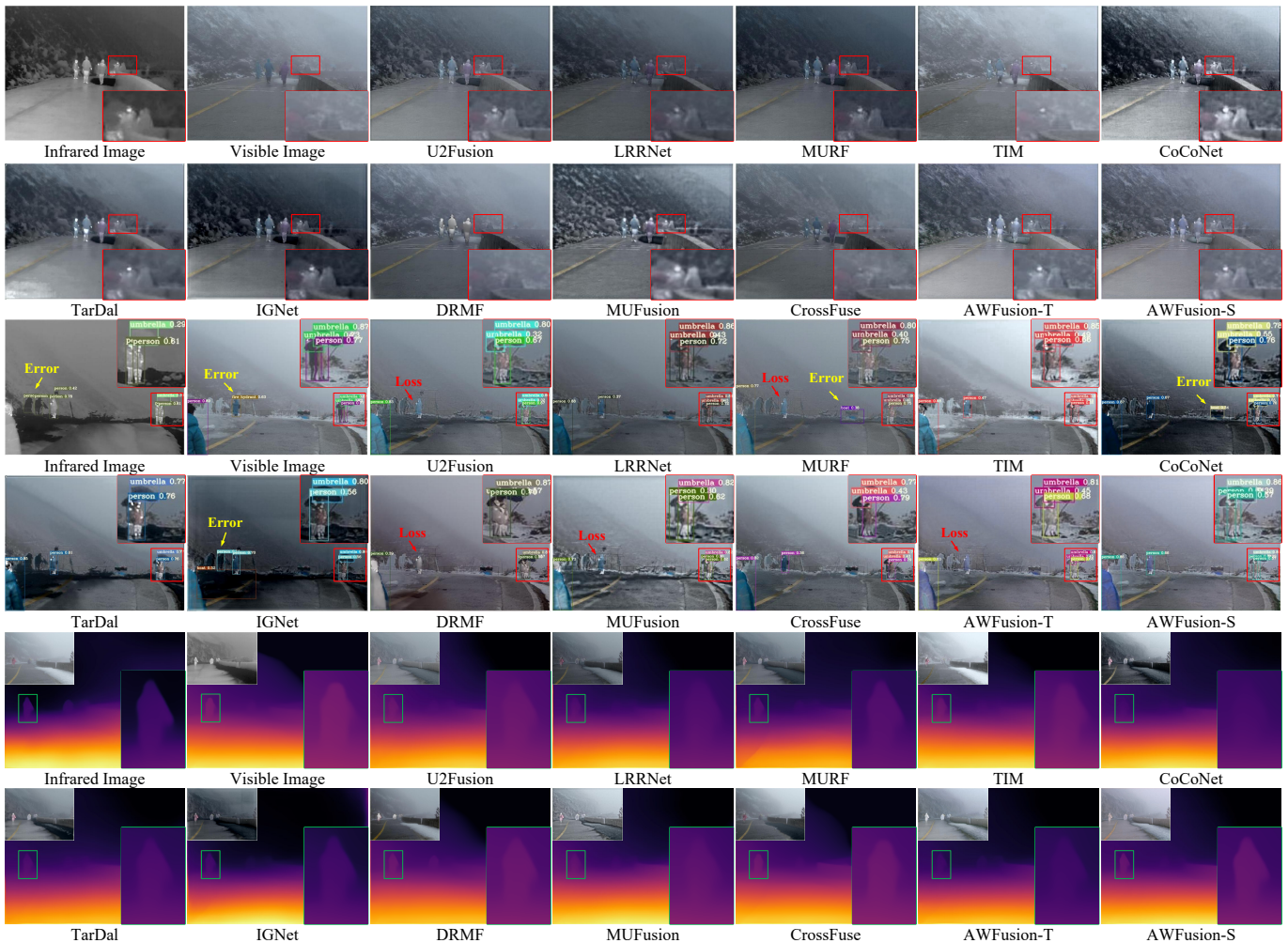


Fig. 9. Comparison of fusion results of all methods in real haze scenes. The first and second rows present fusion performance comparison experiments, the third and fourth rows show object detection accuracy comparisons, and the fifth and sixth rows display depth estimation comparison experiments.

unknown real scenes. By examining the accuracies of different methods in the object detection task, it is clear that only the AWFusion-S results successfully detect all target information in the scene. While the CoCoNet method enhances target information, this also introduces detection errors, suggesting that blind enhancement is not an effective solution to the problem of degraded fusion. The proposed algorithm effectively recovers scene details and integrates complementary multi-modality information, achieving the highest detection accuracy across all objects. For the depth estimation task, the results visualize each ability of method to extract overall scene information. While all methods preserved depth in the foreground, many, such as U2Fusion, LRRNet, CoCoNet, and MUFusion, struggled with accurate depth estimation for distant pedestrians obscured by haze. Additionally, haze affected the performance of TIM, IGSNet, and DRMF, as these methods failed to maintain contrast between the roadside fence and its surroundings, leading to edge blurring in the depth map.

In summary, the proposed algorithm outperforms current SOTA methods in both fusion performance and semantic information retention when addressing real-world scene challenges. It demonstrates excellent performance in downstream tasks,

such as object detection and depth estimation, indicating its high practical application value in real-world.

#### D. Quantitative Comparison

1) *Fusion Performance Comparison*: We selected 50 pairs of infrared and visible source images from the AWMM 100k dataset for each of the three types of adverse weather: rain, haze, and snow, as the test set. The ground truth corresponding to the degraded images was used as input for all comparison methods. Table II presents the results of all methods across nine objective metrics, with the first column indicating the source image types used by each method. The top three scores for each metric are highlighted. Notably, Table II shows that the proposed method, even when performing fusion under adverse weather conditions, outperforms comparison methods operating under ideal conditions. In rain, haze, and snow, the proposed teacher model ranks in the top three for eight or more metrics, while the student model ranks in the top three for 7, 4, and 7 metrics, respectively.

By specifically analyzing the scores of each metric, we can draw the following conclusions:

TABLE II

QUANTITATIVE COMPARISON RESULTS OF ALL ALGORITHMS IN THREE WEATHER CONDITIONS (RAIN, HAZE AND SNOW). **BOLD** IS THE BEST, **RED** IS THE SECOND AND **BLUE** IS THE THIRD.

Source	Method	Pub.	$Q_G\uparrow$	$Q_M\uparrow$	$Q_S\uparrow$	$Q_{CB}\uparrow$	$Q_{CV}\downarrow$	$Q^{AB/F}\uparrow$	$SSIM\uparrow$	$SCD\uparrow$	$EN\uparrow$
GT	U2Fusion [2]	<i>TPAMI 2020</i>	0.2548	0.4524	0.7769	0.4565	901.4884	0.2985	0.3631	1.0276	4.4955
	LRRNet [4]	<i>TPAMI 2023</i>	0.3194	0.5046	0.7003	0.3593	682.5369	0.4250	0.1708	0.7897	5.8903
	MURF [38]	<i>TPAMI 2023</i>	0.2570	0.3839	0.5732	0.3218	1523.9926	0.2285	0.2699	0.9151	4.5988
	TIM [35]	<i>TPAMI 2024</i>	0.2057	0.3498	0.4630	0.3844	827.1437	0.3035	0.1585	0.9651	6.1997
	CoCoNet [50]	<i>IJCV 2023</i>	0.1526	0.2232	0.4021	0.4530	1099.7753	0.2129	0.1756	1.3002	<b>7.6143</b>
	TarDal [3]	<i>CVPR 2022</i>	<b>0.3563</b>	0.3859	0.5739	0.2710	<b>653.6011</b>	0.3826	0.3053	1.5556	6.2024
	IGNet [32]	<i>MM 2023</i>	0.3529	0.4921	0.7232	0.4570	919.9543	0.4420	0.3515	<b>1.5791</b>	6.0812
	DRMF [51]	<i>MM 2024</i>	0.3108	0.4170	0.5844	<b>0.5292</b>	929.2306	0.3555	0.2743	0.8937	6.2728
	MUFusion [52]	<i>InfFus 2023</i>	0.3438	0.4696	<b>0.7860</b>	<b>0.5102</b>	1039.5903	0.4199	<b>0.3959</b>	1.4061	5.6906
	CrossFuse [53]	<i>InfFus 2024</i>	<b>0.4057</b>	<b>0.5718</b>	0.7132	0.4655	1840.1690	<b>0.4648</b>	<b>0.3832</b>	1.0081	5.9859
Rain	AWFusion-T	-	<b>0.3582</b>	<b>0.6855</b>	<b>0.8444</b>	0.4613	<b>464.7867</b>	<b>0.4839</b>	<b>0.3693</b>	<b>1.6311</b>	<b>6.3160</b>
	AWFusion-S	-	0.3334	<b>0.6428</b>	<b>0.8335</b>	<b>0.4691</b>	<b>476.3436</b>	<b>0.4618</b>	0.3528	<b>1.6010</b>	<b>6.2777</b>
GT	U2Fusion [2]	<i>TPAMI 2020</i>	0.3654	0.4275	0.7236	<b>0.5051</b>	840.3653	0.4086	0.3911	1.1512	5.7205
	LRRNet [4]	<i>TPAMI 2023</i>	0.4154	0.4775	<b>0.7646</b>	0.4455	463.4354	<b>0.5218</b>	0.3046	0.8130	6.6553
	MURF [38]	<i>TPAMI 2023</i>	0.2589	0.3324	0.6395	0.4055	1305.4273	0.2277	0.3124	0.9431	5.3601
	TIM [35]	<i>TPAMI 2024</i>	0.3020	0.3983	0.6499	0.4135	507.1376	0.4078	0.2833	0.8978	<b>7.1141</b>
	CoCoNet [50]	<i>IJCV 2023</i>	0.2664	0.2446	0.6157	0.4647	556.1065	0.3547	0.2987	<b>1.4288</b>	<b>7.6564</b>
	TarDal [3]	<i>CVPR 2022</i>	0.4109	0.3832	0.7308	0.3710	<b>337.3376</b>	0.4366	<b>0.4009</b>	<b>1.4207</b>	6.8040
	IGNet [32]	<i>MM 2023</i>	0.3271	0.4117	0.5225	0.4234	1293.6847	0.4110	0.2683	<b>1.4465</b>	6.2330
	DRMF [51]	<i>MM 2024</i>	<b>0.5203</b>	<b>0.6138</b>	0.7530	0.4463	477.8087	0.5026	<b>0.4182</b>	1.0414	6.5732
	MUFusion [52]	<i>InfFus 2023</i>	0.3629	0.4200	0.7236	<b>0.4908</b>	2079.8455	0.4451	0.3723	1.2420	6.5892
	CrossFuse [53]	<i>InfFus 2024</i>	<b>0.4542</b>	0.5423	0.7301	0.4559	2474.6507	0.4847	0.3850	0.9437	6.5648
Haze	AWFusion-T	-	<b>0.4497</b>	<b>0.5889</b>	<b>0.7949</b>	<b>0.4838</b>	<b>374.9215</b>	<b>0.5585</b>	<b>0.4078</b>	1.2209	<b>6.9558</b>
	AWFusion-S	-	0.4283	<b>0.5471</b>	<b>0.7738</b>	0.4610	<b>462.8585</b>	<b>0.5322</b>	0.3901	1.1719	6.9469
GT	U2Fusion [2]	<i>TPAMI 2020</i>	0.3035	0.4330	<b>0.7349</b>	0.4547	1031.8395	0.3606	0.3666	1.0589	5.1796
	LRRNet [4]	<i>TPAMI 2023</i>	0.3574	0.4651	0.7154	0.3737	661.1762	<b>0.4719</b>	0.2361	0.8301	6.1878
	MURF [38]	<i>TPAMI 2023</i>	0.2440	0.3547	0.5581	0.3482	1613.7692	0.2180	0.2676	0.8499	5.0984
	TIM [35]	<i>TPAMI 2024</i>	0.2433	0.3626	0.5181	0.3739	820.5891	0.3465	0.2105	0.8977	6.5951
	CoCoNet [50]	<i>IJCV 2023</i>	0.2420	0.2580	0.5238	0.4512	828.9278	0.3277	0.2593	1.4450	<b>7.5726</b>
	TarDal [3]	<i>CVPR 2022</i>	0.3511	0.3718	0.6238	0.2903	<b>553.2230</b>	0.4171	0.3453	1.4684	6.4487
	IGNet [32]	<i>MM 2023</i>	0.3268	0.4577	0.5938	0.4324	1141.8494	0.4356	0.2986	<b>1.5142</b>	6.0336
	DRMF [51]	<i>MM 2024</i>	<b>0.3948</b>	0.4684	0.6747	<b>0.5055</b>	729.0171	0.4649	0.3417	1.2065	6.2139
	MUFusion [52]	<i>InfFus 2023</i>	0.3543	0.4336	0.7342	<b>0.4953</b>	1699.4374	0.4372	<b>0.3787</b>	1.2984	6.1981
	CrossFuse [53]	<i>InfFus 2024</i>	<b>0.4090</b>	<b>0.5187</b>	0.6995	0.4567	2421.3634	0.4507	0.3724	0.9919	6.1354
Snow	AWFusion-T	-	<b>0.3580</b>	<b>0.5591</b>	<b>0.8179</b>	<b>0.4827</b>	<b>246.8077</b>	<b>0.4985</b>	<b>0.3780</b>	<b>1.5700</b>	<b>6.6173</b>
	AWFusion-S	-	0.3552	<b>0.5535</b>	<b>0.8119</b>	0.4798	<b>270.1595</b>	<b>0.4937</b>	<b>0.3734</b>	<b>1.4937</b>	<b>6.6531</b>

(1) In the image feature-based metrics  $Q_G$  and  $Q_M$ , which are primarily computed using the Sobel edge operator and two-level Haar wavelet, respectively, these metrics assess the edge information in the fusion results. The proposed algorithm achieves high scores in both, indicating that AWFusion preserves the edge structure while effectively removing degradation (such as haze) that significantly obscures edges.

(2) Analyzing the  $SSIM$  and  $SCD$  metrics, it is worth noting that AWFusion-S performs slightly worse in rain and haze scenes compared to snow on the  $SSIM$  metric. This discrepancy arises because rain and haze are continuously distributed degradations, while snow is more localized. As a result, snow is slightly easier to process than rain and haze. The proposed algorithm does not rank among the top three in the  $SCD$  metric for haze scenes. This metric evaluates image quality based on texture, local structural changes, and noise sensitivity, suggesting that the performance of algorithm in extracting local texture under haze is somewhat weaker than in other conditions.

(3) For the metrics  $Q_{CB}$  and  $Q_{CV}$ , which are inspired by human perception, the proposed method performs exceptionally well. This aligns with the results shown in Figs. 5 to 7 and

Fig. 9, where the method effectively integrates multi-modality information while eliminating interference, ensuring that the fusion results are not distorted by adverse weather or enhanced in ways that conflict with human visual perception.

In summary, the performance of the proposed algorithm in quantitative comparisons further validates its practical value in handling severe weather conditions, demonstrating excellent fusion capabilities.

2) *Semantic Segmentation Performance Comparison:* The proposed all-weather MMIF algorithms are designed to support real-world applications, such as autonomous driving, surveillance, and UAV navigation. In these scenarios, the goal is not just to generate visually enhanced images but to enable effective decision-making and analysis (e.g., object detection, semantic segmentation) from the fused images. To comprehensively evaluate the fusion performance under three types of severe weather, we introduced a downstream task. In Table III, we compare the performance of various algorithms using BANet [61] as the segmentation network. Unlike comparison methods, which receive clean source images as input, the proposed algorithm performs fusion under severe weather conditions. As shown in Table III, the proposed algorithm

TABLE III

COMPARISON OF SEGMENTATION ACCURACIES FOR ALL METHODS ACROSS DIFFERENT CATEGORIES IN THE MSRS DATASET. BANET IS USED AS THE SEGMENTATION NETWORK. **BOLD** IS THE BEST, **RED** IS THE SECOND AND **BLUE** IS THE THIRD.

Source	Method	Pub.	Background	Car	Person	Bike	Curve	Car Stop	Cuardrail	Color cone	Bump	mIoU
GT	U2Fusion [2]	<i>TPAMI 2020</i>	98.39	92.88	73.25	73.03	52.82	73.75	86.2	40.31	83.2	74.87
	LRRNet [4]	<i>TPAMI 2023</i>	98.51	93.18	69.62	73.89	65.18	77.95	84.59	35.95	88.96	76.43
	MURF [38]	<i>TPAMI 2023</i>	99.13	95.56	<b>83.54</b>	86.65	76.27	88.21	<b>93.48</b>	76.25	90.59	87.74
	TIM [35]	<i>TPAMI 2024</i>	98.22	91.17	67.94	69.4	59.53	67.74	83.42	30.59	85.59	72.62
	CoCoNet [50]	<i>IJCV 2023</i>	98.3	92.03	69.31	70.66	57.72	73.62	87.49	29.44	84.9	73.72
	TarDal [3]	<i>CVPR 2022</i>	98.39	92.29	70	68.47	62.07	74.59	87.9	35.65	85.42	75.01
	IGNet [32]	<i>MM 2023</i>	99.12	95.61	83.09	87.22	74.97	87.96	93.1	76.13	90.9	87.6
	DRMF [51]	<i>MM 2024</i>	99.16	95.14	82.36	<b>88.2</b>	84.27	<b>90.68</b>	91.67	<b>80.35</b>	<b>92.08</b>	<b>89.32</b>
	MUFusion [52]	<i>InfFus 2023</i>	<b>99.23</b>	95.17	<b>83.84</b>	<b>88.43</b>	84.1	88.9	92.94	<b>80.7</b>	86.12	88.82
	CrossFuse [53]	<i>InfFus 2024</i>	98.04	90.3	67.43	68.51	58.58	71.81	68.13	29.92	68.7	69.04
Rain	AWFusion-S	-	<b>99.32</b>	<b>96.49</b>	<b>84.77</b>	<b>88.76</b>	<b>86.35</b>	<b>90.45</b>	<b>93.91</b>	<b>78.45</b>	91.82	<b>90.04</b>
Haze			99.19	<b>95.69</b>	81.51	81.94	<b>85.21</b>	89.5	91.57	72.73	<b>93.57</b>	87.88
Snow			<b>99.25</b>	<b>95.92</b>	81.24	86.4	<b>86.77</b>	<b>90.36</b>	<b>93.74</b>	78.04	<b>92.32</b>	<b>89.34</b>

TABLE IV

COMPARISON OF DETECTION ACCURACY OF ALL METHODS ON M3FD DATASET. WE USED YOLOV7 AS A DETECTOR. **BOLD** IS THE BEST, **RED** IS THE SECOND AND **BLUE** IS THE THIRD.

Source	Method	Pub.	People	Car	Bus	Lamp	Motorcycle	Truck	mAP@0.5	mAP@[0.5:0.95]
GT	U2Fusion [2]	<i>TPAMI 2020</i>	<b>0.816</b>	0.903	0.901	0.716	<b>0.711</b>	0.801	<b>0.808</b>	<b>0.512</b>
	LRRNet [4]	<i>TPAMI 2023</i>	0.785	<b>0.909</b>	<b>0.912</b>	<b>0.764</b>	<b>0.721</b>	<b>0.808</b>	<b>0.817</b>	0.484
	MURF [38]	<i>TPAMI 2023</i>	<b>0.815</b>	0.885	0.881	0.711	0.675	0.8	0.794	0.498
	TIM [35]	<i>TPAMI 2024</i>	0.731	0.898	0.878	0.657	0.656	0.769	0.765	0.48
	CoCoNet [50]	<i>IJCV 2023</i>	0.791	0.889	0.889	0.696	0.641	0.762	0.778	0.49
	TarDal [3]	<i>CVPR 2022</i>	0.792	0.877	0.857	0.585	0.62	0.713	0.741	0.462
	IGNet [32]	<i>MM 2023</i>	0.793	0.859	0.836	0.532	0.554	0.721	0.716	0.439
	DRMF [51]	<i>MM 2024</i>	0.699	0.897	0.896	<b>0.787</b>	0.697	0.784	0.793	0.494
	MUFusion [52]	<i>InfFus 2023</i>	<b>0.803</b>	<b>0.906</b>	<b>0.908</b>	0.734	0.694	<b>0.802</b>	<b>0.808</b>	<b>0.507</b>
	CrossFuse [53]	<i>InfFus 2024</i>	0.692	0.891	0.871	0.671	0.674	0.771	0.762	0.473
	AWFusion-S	-	0.791	<b>0.922</b>	<b>0.93</b>	<b>0.804</b>	<b>0.726</b>	<b>0.821</b>	<b>0.832</b>	<b>0.534</b>

ranks first in mean intersection-over-union (mIoU) for rain scenes and second for snow scenes. Although the mIoU score for the haze scenario is not in the top three, it still secures fifth place. These experiments demonstrate that the proposed algorithm retains high-level semantic information in scenes with interference and accurately recognizes key targets such as roads, pedestrians, and vehicles.

3) *Object Detection Performance Comparison*: In real-world applications, systems must adapt to varying weather and environmental conditions. Although our method is tailored for severe weather, it also delivers high-quality fusion results in normal conditions, such as clear, haze-free, and rain-free environments. This demonstrates not only its effectiveness in harsh weather but also its strong generalization ability in clean settings. In Table IV, we evaluated the object detection accuracies of all methods on the M3FD dataset using YOLOv7 [10]. As shown in Table IV, the proposed algorithm achieves the highest detection accuracy across all five categories, with both mAP@0.5 and mAP@[0.5:0.95] also obtaining the top scores. These results confirm that the proposed algorithm retains sufficient information and detail for accurate localization and identification in object detection. Moreover, it enhances detection accuracy by preserving and leveraging complementary information.

#### E. Extension to Multiple Adverse Weather Disturbances

Compound degradation increases scene complexity, as rain, haze, and snow exhibit distinct physical characteristics: rain

and snow cause localized occlusion, while haze reduces overall contrast. When combined, these effects create more challenging degradation. Although specific patterns can address individual disturbances, the model must exhibit strong adaptability and generalization to handle multiple disturbances simultaneously. To evaluate the generalization ability of the proposed algorithm under severe weather conditions, we conducted extended experiments with composite degradation. We used DT [62] as a preprocessing model to remove interference from visible images. In the comparison method, fusion is performed on the preprocessed image, while the proposed algorithm directly processes the fusion result on the original source image. As shown in Fig. 10, when two disturbances coexist in the source image, DT can only address one at a time, despite its effectiveness handle individual interferences. The residual degradation is carried over to the fusion result, leading to suboptimal outcomes. In contrast, the proposed method reconstructs high-fidelity scene details under complex weather conditions, preserving key features while avoiding issues like insufficient brightness or information loss.

#### F. Ablation Experiment

We performed an ablation analysis on the six modules to verify their individual roles and effectiveness. The modules were grouped into four experimental sets, with the results visualized in Fig. 11 and quantitatively compared in Table V.

1) *Effectiveness Analysis of the Fusion Module*: The image fusion module plays a critical role in the end-to-end framework

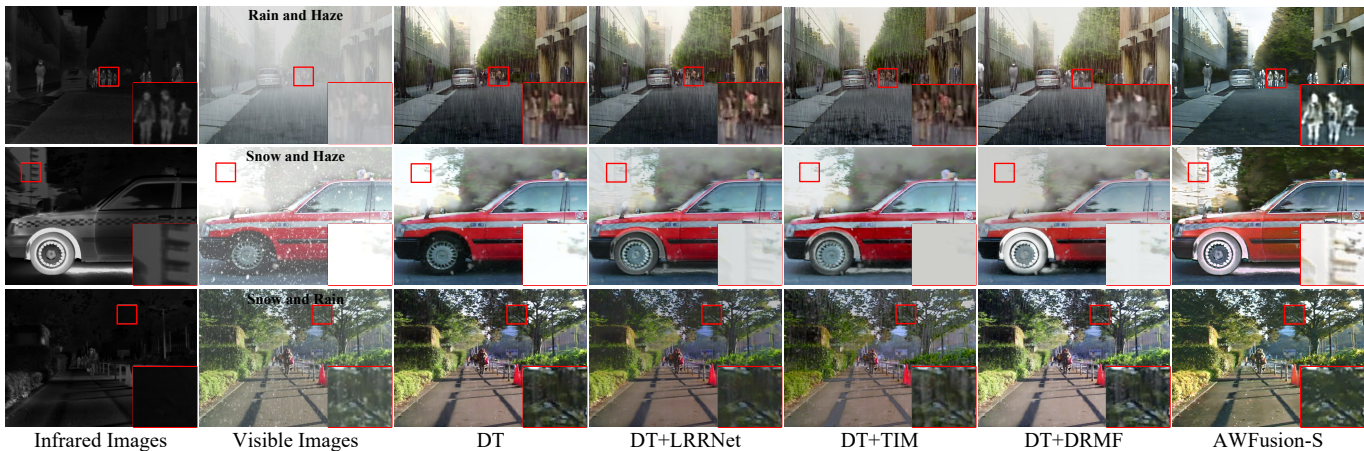


Fig. 10. Comparison of fusion results of different methods under multiple adverse weather disturbances.

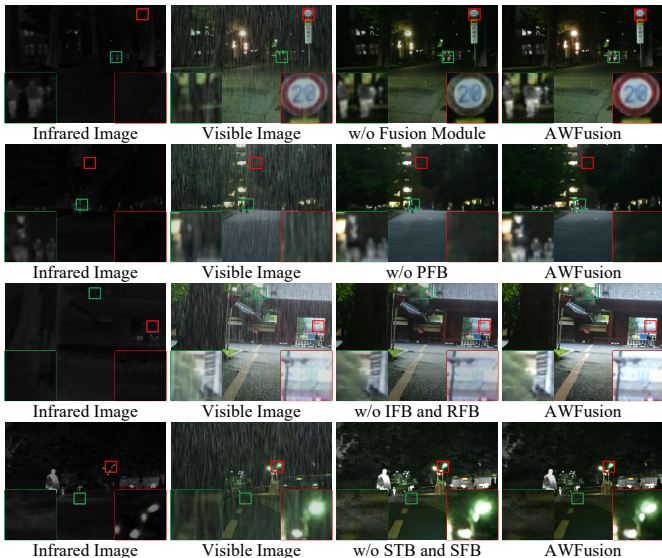


Fig. 11. Qualitative comparison of ablation experiments under rain weather.

by enabling multi-modality feature interaction. To evaluate its effectiveness, we performed an ablation analysis. As illustrated in the first row of Fig. 11, removing the fusion module disrupts this interaction, causing salient infrared features to be occluded by blurred visible details, as seen in the green zoomed-in area. Additionally, the absence of feature interaction introduces low-contrast IR information into the fusion output, making it difficult to reconstruct color information and resulting in slight color distortion, highlighted in the red zoomed-in area.

2) *Effectiveness Analysis of the PFB*: The PFB module, built on the atmospheric scattering model, effectively mitigates weather-induced interference and reconstructs clear scene features. We performed an ablation analysis. As shown in the second row of Fig. 11, removing the PFB module leaves residual degradation in the fusion result. In texture-rich regions, such as leaves, the network struggles to distinguish between degradation artifacts and actual textures, as highlighted in the red zoomed-in area, leading to detail loss and blurred edges.

TABLE V  
QUANTITATIVE COMPARISON OF ABLATION EXPERIMENTS IN RAIN WEATHER. **BOLD** IS THE BEST.

	$Q_M$	$Q_S$	$Q_{CV}$	$SSIM$	$EN$
w/o PFB	0.5439	0.7917	579.3986	0.3048	6.2609
w/o Fusion	0.4989	0.7953	577.4851	0.2165	6.2930
w/o IFB and RFB	0.4646	0.8096	501.8484	0.2923	5.9288
w/o STB and SFB	0.5454	0.7979	536.2539	0.3904	<b>6.7516</b>
AWFusion	<b>0.6855</b>	<b>0.8444</b>	<b>464.7867</b>	<b>0.3993</b>	6.3160

3) *Effectiveness Analysis of the IFB and RFB*: To improve the ability of network to estimate light transmission, we designed the IFB and RFB modules based on retina theory and constrained feature generation by reconstructing the loss. As shown in the third row of Fig. 11, removing these modules results in reduced lighting in the fusion output, likely due to inaccurate transmission map estimation and insufficient luminance compensation. This makes the absence of light recovery more noticeable. Additionally, Fig. 4 shows a significant drop in the  $Q_M$ ,  $SSIM$ , and  $EN$  metrics.

4) *Effectiveness Analysis of the Fusion Strategies*: To leverage the low-rank and sparse features decomposed by the LLRR block, we designed the SFB to fuse sparse components and the STB to integrate low-rank components through context extraction. An ablation study was performed by removing the SFB and STB, replacing them with a maximum-value fusion strategy. As more feature channels are extracted from the source image, the simple fusion strategy impedes effective cross-modal interaction, restricting the extraction of salient and complementary features. This causes pixel redundancy in the fused output, reflected in the excessively high  $EN$  metric in Table V. The enlarged region in Fig. 11 further highlights increased noise in ground, complicating object recognition.

## V. CONCLUSION

In this study, we propose an all-weather MMIF method, focusing on the relationship between multi-modality image fusion and image restoration. Our framework shifts the network’s objective from pixel-perfect recovery to maximizing the representation of key scene information. The end-to-end

design comprises two main modules: a fusion module and a restoration module. The fusion module decouples features from multiple modalities into low-rank and sparse components, which are merged interactively using specialized fusion strategies. Guided by a physical model, the restoration module restores clear details from blur pixels, ensuring high-quality fusion results. Additionally, we introduce a large-scale benchmark dataset, AWMM-100k, tailored for multi-modality image processing under adverse weather conditions. Experimental results confirm that the AWFusion surpasses existing methods in both adverse and normal conditions, with outstanding performance in downstream tasks, demonstrating its strong practical value.

## REFERENCES

- [1] X. Zhang and Y. Demiris, "Visible and infrared image fusion using deep learning," *IEEE Trans. Pattern Anal. Mach. Intell.*, vol. 45, no. 8, pp. 10 535–10 554, 2023.
- [2] Z. Zhao, H. Bai, J. Zhang, Y. Zhang, S. Xu, Z. Lin, R. Timofte, and L. Van Gool, "Cddfuse: Correlation-driven dual-branch feature decomposition for multi-modality image fusion," in *IEEE Conf. Comput. Vis. Pattern Recog.*, 2023, pp. 5906–5916.
- [3] J. Liu, X. Fan, Z. Huang, G. Wu, R. Liu, W. Zhong, and Z. Luo, "Target-aware dual adversarial learning and a multi-scenario multi-modality benchmark to fuse infrared and visible for object detection," in *IEEE Conf. Comput. Vis. Pattern Recog.*, 2022, pp. 5802–5811.
- [4] H. Li, T. Xu, X.-J. Wu, J. Lu, and J. Kittler, "Lrrnet: A novel representation learning guided fusion network for infrared and visible images," *IEEE Trans. Pattern Anal. Mach. Intell.*, 2023.
- [5] H. Li, J. Liu, Y. Zhang, and Y. Liu, "A deep learning framework for infrared and visible image fusion without strict registration," *Int. J. Comput. Vis.*, vol. 132, p. 1625–1644, 2024.
- [6] J. Li, H. Dai, H. Han, and Y. Ding, "Mseg3d: Multi-modal 3d semantic segmentation for autonomous driving," in *IEEE Conf. Comput. Vis. Pattern Recog.*, 2023, pp. 21 694–21 704.
- [7] L.-C. Chen, G. Papandreou, I. Kokkinos, K. Murphy, and A. L. Yuille, "Deepplab: Semantic image segmentation with deep convolutional nets, atrous convolution, and fully connected crfs," *IEEE Trans. Pattern Anal. Mach. Intell.*, vol. 40, no. 4, pp. 834–848, 2017.
- [8] L.-C. Chen, Y. Zhu, G. Papandreou, F. Schroff, and H. Adam, "Encoder-decoder with atrous separable convolution for semantic image segmentation," in *Eur. Conf. Comput. Vis.*, 2018, pp. 801–818.
- [9] V. VS, P. Oza, and V. M. Patel, "Towards online domain adaptive object detection," 2023, pp. 478–488.
- [10] C.-Y. Wang, A. Bochkovskiy, and H.-Y. M. Liao, "Yolov7: Trainable bag-of-freebies sets new state-of-the-art for real-time object detectors," in *IEEE Conf. Comput. Vis. Pattern Recog.*, 2023, pp. 7464–7475.
- [11] A. Bochkovskiy, C.-Y. Wang, and H.-Y. M. Liao, "Yolov4: Optimal speed and accuracy of object detection," *arXiv preprint arXiv:2004.10934*, 2020.
- [12] Y. Xiao, F. Codevilla, A. Gurram, O. Urfalioglu, and A. M. López, "Multimodal end-to-end autonomous driving," *IEEE Trans. Intell. Transp. Syst.*, vol. 23, no. 1, pp. 537–547, 2020.
- [13] Z. Le, J. Huang, H. Xu, F. Fan, Y. Ma, X. Mei, and J. Ma, "Uifgan: An unsupervised continual-learning generative adversarial network for unified image fusion," *Inf. Fusion*, vol. 88, pp. 305–318, 2022.
- [14] J. Ma, H. Zhang, Z. Shao, P. Liang, and H. Xu, "Ganmcc: A generative adversarial network with multiclassification constraints for infrared and visible image fusion," *IEEE Trans. Instrum. Meas.*, vol. 70, pp. 1–14, 2020.
- [15] Y. Fu, X.-J. Wu, and T. Durrani, "Image fusion based on generative adversarial network consistent with perception," *Inf. Fusion*, vol. 72, pp. 110–125, 2021.
- [16] H. Zhou, W. Wu, Y. Zhang, J. Ma, and H. Ling, "Semantic-supervised infrared and visible image fusion via a dual-discriminator generative adversarial network," *IEEE Trans. Multimedia*, 2021.
- [17] J. Ma, L. Tang, F. Fan, J. Huang, X. Mei, and Y. Ma, "Swinfusion: Cross-domain long-range learning for general image fusion via swin transformer," *IEEE/CAA J. Autom. Sinica*, vol. 9, no. 7, pp. 1200–1217, 2022.
- [18] W. Tang, F. He, and Y. Liu, "Tccfusion: An infrared and visible image fusion method based on transformer and cross correlation," vol. 137, p. 109295, 2023.
- [19] X. Deng and P. L. Dragotti, "Deep convolutional neural network for multi-modal image restoration and fusion," *IEEE Trans. Pattern Anal. Mach. Intell.*, vol. 43, no. 10, pp. 3333–3348, 2020.
- [20] X. Chen, H. Li, M. Li, and J. Pan, "Learning a sparse transformer network for effective image deraining," in *IEEE Conf. Comput. Vis. Pattern Recog.*, 2023, pp. 5896–5905.
- [21] Y. Zheng, J. Zhan, S. He, J. Dong, and Y. Du, "Curricular contrastive regularization for physics-aware single image dehazing," in *IEEE Conf. Comput. Vis. Pattern Recog.*, 2023, pp. 5785–5794.
- [22] J. Dong and J. Pan, "Physics-based feature dehazing networks," in *Eur. Conf. Comput. Vis.* Springer, 2020, pp. 188–204.
- [23] H. Sreter and R. Giryes, "Learned convolutional sparse coding," in *ICASSP. IEEE*, 2018, pp. 2191–2195.
- [24] L. Jian, X. Yang, Z. Liu, G. Jeon, M. Gao, and D. Chisholm, "Sedrfuse: A symmetric encoder-decoder with residual block network for infrared and visible image fusion," *IEEE Trans. Instrum. Meas.*, vol. 70, pp. 1–15, 2020.
- [25] J. Ma, W. Yu, P. Liang, C. Li, and J. Jiang, "Fusiongan: A generative adversarial network for infrared and visible image fusion," *Inf. Fusion*, vol. 48, pp. 11–26, 2019.
- [26] M. Xu, L. Tang, H. Zhang, and J. Ma, "Infrared and visible image fusion via parallel scene and texture learning," vol. 132, p. 108929, 2022.
- [27] F. Zhao, W. Zhao, and H. Lu, "Interactive feature embedding for infrared and visible image fusion," *IEEE Trans. Neural Netw. Learn. Syst.*, 2023.
- [28] H. Xu, J. Ma, J. Jiang, X. Guo, and H. Ling, "U2fusion: A unified unsupervised image fusion network," *IEEE Trans. Pattern Anal. Mach. Intell.*, vol. 44, no. 1, pp. 502–518, 2020.
- [29] S. Peng, C. Guo, X. Wu, and L.-J. Deng, "U2net: A general framework with spatial-spectral-integrated double u-net for image fusion," in *ACM Int. Conf. Multimedia*, 2023, pp. 3219–3227.
- [30] Y. Guan, R. Xu, M. Yao, L. Wang, and Z. Xiong, "Mutual-guided dynamic network for image fusion," in *ACM Int. Conf. Multimedia*, 2023, pp. 1779–1788.
- [31] Z. Zhao, H. Bai, J. Zhang, Y. Zhang, K. Zhang, S. Xu, D. Chen, R. Timofte, and L. Van Gool, "Equivariant multi-modality image fusion," in *IEEE Conf. Comput. Vis. Pattern Recog.*, 2024, pp. 25 912–25 921.
- [32] J. Li, J. Chen, J. Liu, and H. Ma, "Learning a graph neural network with cross modality interaction for image fusion," in *ACM Int. Conf. Multimedia*, 2023, pp. 4471–4479.
- [33] L. Tang, J. Yuan, and J. Ma, "Image fusion in the loop of high-level vision tasks: A semantic-aware real-time infrared and visible image fusion network," *Inf. Fusion*, vol. 82, pp. 28–42, 2022.
- [34] Z. Liu, J. Liu, B. Zhang, L. Ma, X. Fan, and R. Liu, "Paif: Perception-aware infrared-visible image fusion for attack-tolerant semantic segmentation," in *ACM Int. Conf. Multimedia*, 2023, pp. 3706–3714.
- [35] R. Liu, Z. Liu, J. Liu, X. Fan, and Z. Luo, "A task-guided, implicitly-searched and metainitialized deep model for image fusion," *IEEE Trans. Pattern Anal. Mach. Intell.*, 2024.
- [36] H. Li, J. Zhao, J. Li, Z. Yu, and G. Lu, "Feature dynamic alignment and refinement for infrared-visible image fusion: Translation robust fusion," *Inf. Fusion*, vol. 95, pp. 26–41, 2023.
- [37] Z. Huang, J. Liu, X. Fan, R. Liu, W. Zhong, and Z. Luo, "Reconet: Recurrent correction network for fast and efficient multi-modality image fusion," in *Eur. Conf. Comput. Vis.* Springer, 2022, pp. 539–555.
- [38] H. Xu, J. Yuan, and J. Ma, "Murf: Mutually reinforcing multi-modal image registration and fusion," *IEEE Trans. Pattern Anal. Mach. Intell.*, 2023.
- [39] H. Li, Y. Cen, Y. Liu, X. Chen, and Z. Yu, "Different input resolutions and arbitrary output resolution: A meta learning-based deep framework for infrared and visible image fusion," *IEEE Trans. Image Process.*, vol. 30, pp. 4070–4083, 2021.
- [40] X. Li, F. Zhou, and H. Tan, "Joint image fusion and denoising via three-layer decomposition and sparse representation," *Knowledge-Based Systems*, vol. 224, p. 107087, 2021.
- [41] L. Tang, X. Xiang, H. Zhang, M. Gong, and J. Ma, "Divfusion: Darkness-free infrared and visible image fusion," *Inf. Fusion*, vol. 91, pp. 477–493, 2023.
- [42] X. Yi, H. Xu, H. Zhang, L. Tang, and J. Ma, "Text-if: Leveraging semantic text guidance for degradation-aware and interactive image fusion," in *IEEE Conf. Comput. Vis. Pattern Recog.*, 2024, pp. 27 026–27 035.
- [43] W.-T. Chen, Z.-K. Huang, C.-C. Tsai, H.-H. Yang, J.-J. Ding, and S.-Y. Kuo, "Learning multiple adverse weather removal via two-stage knowledge learning and multi-contrastive regularization: Toward a unified

model,” in *IEEE Conf. Comput. Vis. Pattern Recog.*, 2022, pp. 17 653–17 662.

- [44] Y. Zhu, T. Wang, X. Fu, X. Yang, X. Guo, J. Dai, Y. Qiao, and X. Hu, “Learning weather-general and weather-specific features for image restoration under multiple adverse weather conditions,” in *IEEE Conf. Comput. Vis. Pattern Recog.*, 2023, pp. 21 747–21 758.
- [45] W. Yang, R. T. Tan, J. Feng, J. Liu, Z. Guo, and S. Yan, “Deep joint rain detection and removal from a single image,” in *IEEE Conf. Comput. Vis. Pattern Recog.*, 2017, pp. 1357–1366.
- [46] L. Tang, J. Yuan, H. Zhang, X. Jiang, and J. Ma, “Piafusion: A progressive infrared and visible image fusion network based on illumination aware,” *Inf. Fusion*, vol. 83, pp. 79–92, 2022.
- [47] X. Jia, C. Zhu, M. Li, W. Tang, and W. Zhou, “Llvp: A visible-infrared paired dataset for low-light vision,” in *Int. Conf. Comput. Vis.*, 2021, pp. 3496–3504.
- [48] R.-Q. Wu, Z.-P. Duan, C.-L. Guo, Z. Chai, and C. Li, “Ridcp: Revitalizing real image dehazing via high-quality codebook priors,” in *IEEE Conf. Comput. Vis. Pattern Recog.*, 2023, pp. 22 282–22 291.
- [49] W.-T. Chen, H.-Y. Fang, C.-L. Hsieh, C.-C. Tsai, I. Chen, J.-J. Ding, S.-Y. Kuo *et al.*, “All snow removed: Single image desnowing algorithm using hierarchical dual-tree complex wavelet representation and contradict channel loss,” in *Int. Conf. Comput. Vis.*, 2021, pp. 4196–4205.
- [50] J. Liu, R. Lin, G. Wu, R. Liu, Z. Luo, and X. Fan, “Coconet: Coupled contrastive learning network with multi-level feature ensemble for multi-modality image fusion,” *Int. J. Comput. Vis.*, vol. 132, no. 5, pp. 1748–1775, 2024.
- [51] L. Tang, Y. Deng, X. Yi, Q. Yan, Y. Yuan, and J. Ma, “Drmf: Degradation-robust multi-modal image fusion via composable diffusion prior,” in *ACM Multimedia 2024*.
- [52] C. Cheng, T. Xu, and X.-J. Wu, “Mufusion: A general unsupervised image fusion network based on memory unit,” *Inf. Fusion*, vol. 92, pp. 80–92, 2023.
- [53] H. Li and X.-J. Wu, “Crossfuse: A novel cross attention mechanism based infrared and visible image fusion approach,” *Inf. Fusion*, vol. 103, p. 102147, 2024.
- [54] Z. Liu, E. Blasch, Z. Xue, J. Zhao, R. Laganiere, and W. Wu, “Objective assessment of multiresolution image fusion algorithms for context enhancement in night vision: a comparative study,” *IEEE Trans. Pattern Anal. Mach. Intell.*, vol. 34, no. 1, pp. 94–109, 2011.
- [55] V. Petrovic and C. Xydeas, “Objective image fusion performance characterisation,” in *Int. Conf. Comput. Vis.*, vol. 2. IEEE, 2005, pp. 1866–1871.
- [56] V. Aslantas and E. Bendes, “A new image quality metric for image fusion: The sum of the correlations of differences,” *Aeu-int J. Electron. C.*, vol. 69, no. 12, pp. 1890–1896, 2015.
- [57] R. Ranftl, K. Lasinger, D. Hafner, K. Schindler, and V. Koltun, “Towards robust monocular depth estimation: Mixing datasets for zero-shot cross-dataset transfer,” *IEEE Trans. Pattern Anal. Mach. Intell.*, vol. 44, no. 3, pp. 1623–1637, 2020.
- [58] C.-L. Guo, Q. Yan, S. Anwar, R. Cong, W. Ren, and C. Li, “Image dehazing transformer with transmission-aware 3d position embedding,” in *IEEE Conf. Comput. Vis. Pattern Recog.*, 2022, pp. 5812–5820.
- [59] Y. Song, Z. He, H. Qian, and X. Du, “Vision transformers for single image dehazing,” *IEEE Trans. Image Process.*, vol. 32, pp. 1927–1941, 2023.
- [60] Y. Wang, X. Yan, F. L. Wang, H. Xie, W. Yang, X.-P. Zhang, J. Qin, and M. Wei, “Ucl-dehaze: Towards real-world image dehazing via unsupervised contrastive learning,” *IEEE Trans. Image Process.*, 2024.
- [61] C. Peng, T. Tian, C. Chen, X. Guo, and J. Ma, “Bilateral attention decoder: A lightweight decoder for real-time semantic segmentation,” *Neural Networks*, vol. 137, pp. 188–199, 2021.
- [62] P. W. Patil, S. Gupta, S. Rana, S. Venkatesh, and S. Murala, “Multi-weather image restoration via domain translation,” in *Int. Conf. Comput. Vis.*, 2023, pp. 21 696–21 705.



**Xilai Li** is currently pursuing his bachelor’s degree at the School of Physics and Optoelectronic Engineering, Foshan University, Foshan, China. His research interests include image processing and machine learning.



**Wuyang Liu** is currently pursuing his master’s degree in the Guangdong-Hong Kong-Macau Joint Laboratory of Intelligent Micro-Nano Optoelectronic Technology, School of Physics and Optoelectronic Engineering, Foshan University. His research interests include image processing and machine vision.



**Xiaosong Li** received his Ph.D. in measurement technology and instruments from Beihang University in 2021. He is currently a associate professor with School of Physics and Optoelectronic Engineering, Foshan University, Foshan, China; His research interests include image processing, pattern recognition, and optical metrology.



optical metrology.

**Fuqiang Zhou** received the B.S., M.S., and Ph.D. degrees in test and measurement technology and instruments from Tianjin University, Tianjin, China, in 1994, 1997, and 2000, respectively. He joined the School of Automation Science and Electrical Engineering, Beihang University, Beijing, China, as a Postdoctoral Research Fellow in 2000. He is currently a Professor with the School of Instrumentation and Optoelectronic Engineering, Beihang University. His research interests include precision vision measurement, 3-D vision sensors, image recognition, and



**Huafeng Li** received the M.S. degrees in applied mathematics major from Chongqing University in 2009 and obtained his Ph.D. degree in control theory and control engineering major from Chongqing University in 2012. He is currently a professor at the School of Information Engineering and Automation, Kunming University of Science and Technology, China. His research interests include image processing, computer vision, and information fusion.



more than 45000 times and the H-index is 108. He is now serving as Associate Editor or PC member for several prestigious journals and conferences in the related fields.

**Feiping Nie** received the Ph.D. degree in Computer Science from Tsinghua University, China in 2009, and currently is full professor in Northwestern Polytechnical University, China. His research interests are machine learning and its applications, such as pattern recognition, data mining, computer vision, image processing and information retrieval. He has published more than 300 papers in the following journals and conferences: TPAMI, TIP, TNNLS, TKDE, TFS, ICML, NIPS, KDD, IJCAI, AAAI, ICCV, CVPR, ACM MM. His papers have been cited